J Therm Anal Calorim (2009) 98:197–202
DOI 10.1007/s10973-009-0316-9

Describing temperature increases in plasmon-resonant nanoparticle systems

Michael P. Hoepfner · D. Keith Roper

Received: 14 November 2008 / Accepted: 4 March 2009 / Published online: 25 July 2009

Abstract Plasmon-resonant nanoparticles are being integrated into a variety of actuators, sensors and calorimeters due to their extraordinary optical capabilities. We show a continuum energy balance accurately describes thermal dynamics and equilibrium temperatures in plasmon-resonant nanoparticle systems. Analysis of 18 data sets in which temperature increased $\leq$10.6 °C yielded a mean value of $R^2 > 0.99$. The largest single relative temperature error was 1.11%. A characteristic temperature was introduced into a linear driving force approximation for radiative heat transfer in the continuum energy description to simplify parameter estimation. The maximum percent error of the linearized description rose to 1.5% for the 18 sets. Comparing the two descriptions at simulated temperature increases up to 76.6 °C gave maximum relative errors $\leq$7.16%. These results show for the first time that the energy balance and its linearized approximation are applicable to characterize dynamic and equilibrium temperatures for sensors, actuators and calorimeters containing nanoparticles in microfluidic and lab-on-chip systems over a broad range of heat-transfer lengths, power inputs and corresponding temperature increases.

Keywords Surface plasmon resonance (SPR) · Nanoparticles (NP) · Optothermal photocalorimetry

M. P. Hoepfner
University of Michigan, Ann Arbor, MI, USA

D. K. Roper (✉)
University of Arkansas, Fayetteville, AR, USA
e-mail: dkroper@uark.edu

Introduction

Applications of inorganic colloidal nanocrystals in sensing, analysis and calorimetry are expanding rapidly due to new methods that enable synthesis of nanocrystals at the scale of biomolecules and allow derivatization to use nanocrystals as biosensors and molecular probes. Gold (Au) nanoparticles have been used for DNA identification [1], to discriminate polynucleotide base-pair changes by colorimetry [2] and to enhance Raman spectroscopy [3, 4]. Pump-pulse laser spectroscopy has been applied to examine transient electron dynamics of Au nanoparticles [5–7]. This body of work showed incident resonant photons can be dissipated as heat by way of surface plasmons on noble metal surfaces of suspended nanoparticles or thin films. Recently, the efficiency of converting incident laser light to heat that was subsequently dissipated by nanoparticle suspensions was measured using photocalorimetry [8].

The photocalorimetry data was analyzed by comparing conduction, convection and radiation losses with resonant photon energy used to irradiate thermally-isolated, colloidal-gold nanoparticles in order to calculate the efficiency of converting laser light to heat via surface plasmons. Determining the value of conversion efficiency allowed prediction of transient thermal dynamics and steady-state equilibrium temperature increases $\leq$10.6 °C for effective laser powers between 1.0 and 16.3 mW and for characteristic heat transfer lengths from 4.1 to 66.8 mm. Radiation, the predominant mode of heat transfer at these conditions and a quartic function of temperature [9], was linearized to estimate heat transfer coefficients from the data. But the accuracy of these descriptions were not evaluated and their applicability to a broader range of conditions was not studied.

This study examines the suitability of applying a continuum energy balance to analyze thermal dynamics and

equilibrium temperatures obtained from heat dissipated by surface plasmons in aqueous suspensions of irradiated nanoparticles across a larger range of length scales, power inputs and temperature increases that includes the previous data. We evaluate the accuracy of employing a linearized radiation term to characterize heat transfer for effective power inputs ranging from 11.4 to 102.1 mW, and for characteristic heat transfer lengths ranging from 1.5 to 393.6 mm. These expanded parameter values produce temperature increases from 3.0 to 76.6 °C. We introduce a characteristic temperature into the linearized description that results in a maximum temperature error ≤7.16%. These expressions appear useful to analyze and predict local thermal dynamics and equilibrium temperatures in a wide range of laser-induced surface plasmon resonant heating structures in lab-on-chips [10] and microfluidics. We demonstrate the utility of these expressions by analyzing a sensor in which double-stranded nucleic acid is cyclically denatured at 95 °C and hybridized (annealed) at 55 °C using precise, local control of temperature induced by plasmon-resonant particles [11].

Experiment

Experimental procedure

Photocalorimetric data was obtained by dissipating laser light as heat using an aqueous suspension of nanoparticles as previously described [8]. A schematic of the sample cell can be found in Fig. 1, and the experimental setup is found in Fig. 2. The temperature profile was then analyzed by applying an overall energy balance to evaluate heat transfer from the thermally isolated system.

Overall energy balance and linearization of radiation

The purpose of this study was to examine use of an overall continuum energy balance to describe thermal dynamics

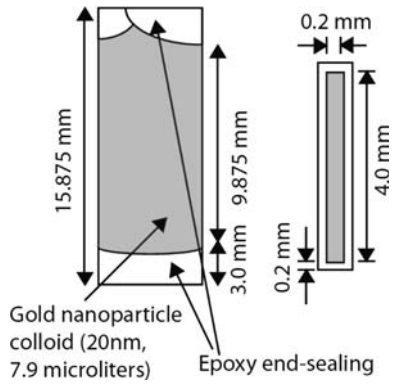

Fig. 1 A schematic and dimensions of the sample cell filled with gold nanoparticle colloid

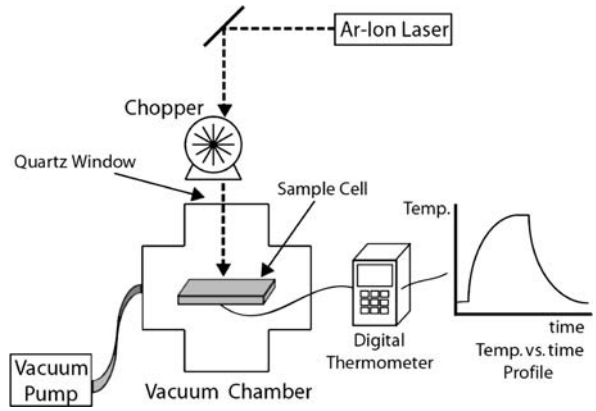

Fig. 2 A schematic of the experimental setup. The energy was provided by the Ar^{+}-Ion laser. Temperature measured by a thermocouple was recorded by a digital thermometer

and temperature equilibria in plasmon resonant nanoparticle systems.

$$\text{System temperature change} = \frac{\text{net heat in}}{\text{thermal mass}} \tag{1}$$

A primary aim was to quantify the error associated with linearizing the radiative heat transfer term in the overall energy balance. Convection was reduced to a negligible amount by suspending the cell in a vacuum ≤1 Torr, leaving only conductive and radiative heat transfer terms in the energy balance. Rapid thermal equilibrium within the nanofluid in the sample cell [8] yields the following complete differential energy balance written in terms of temperature:

$$\frac{dT}{dt} = \frac{1}{\sum mC_P}\left[\eta Q_I - \frac{k_{Air}A_{Samp}}{L_{Air}}(T - T_{Amb}) - \frac{k_{TC}A_{TC}}{L_{TC}}(T - T_{Amb}) - A_{Samp}\varepsilon\sigma(T^4 - T_{Amb}^4)\right] \tag{2}$$

where $\sum mC_P$ is the sum of the products of mass and specific heat of glass, epoxy and aqueous suspension in the sample cell, k_i are thermal conductivities, A_i are surface areas normal to heat transfer, L_i are characteristic heat transfer lengths between the sample and surrounding surfaces at T_{Amb}, A_{Samp} is the surface area of the sample cell, ε is the surface emissivity, σ is the Stefan-Boltzman constant, T is sample cell temperature, and the term ηQ_I represents the fractional value of incident laser light dissipated as heat in the cell. Subscripts i = Air and TC denoted parameters for conduction via air molecules that remained in the vacuum cell and via thermocouple wires, respectively. Equation 2 was linearized using the form:

$$\frac{dT}{dt} = \frac{1}{\sum mC_P}[\eta Q_I - U(T - T_{Amb})] \tag{3}$$

where U is an overall heat transfer coefficient defined as:

$$U \equiv \sum_i \frac{k_i A_i}{L_i} + A_{\text{Samp}}\sigma\varepsilon\left(T^2 + T_{\text{Amb}}^2\right)\left(T' + T_{\text{Amb}}\right) \quad (4)$$

We introduce here a characteristic temperature, T', which is intermediate between T_{Amb} and T_{Equil} and is defined by:

$$T' \equiv f_{\Delta T} T_{\text{Equil}} + (1 - f_{\Delta T}) T_{\text{Amb}} \quad (5)$$

where T_{Equil} is the temperature at which the system equilibrates for given values of ηQ_{I} and L_{Air}, and $f_{\Delta T}$ is a fractional relative difference between T_{Amb} and T_{Equil} which minimizes the maximum relative error between Eqs. 2 and 3.

Criteria for evaluating error of linearized description

The first criterion for evaluating errors between measurements, Eqs. 2, and 3 was the sum of squares of the errors, σ_i, given by [12]:

$$\sigma_i = \sum \left(T_i - T_{\text{Ref}}\right)^2 \quad (6)$$

where T_{Ref} is a reference temperature, subscript i denotes the temperature predicted by either the complete model, $i = 2$, or the linearized model, $i = 3$, and the sum is taken over a complete data set that consists of one temperature point per second for a period on the order of 10^3 s. The sum squared error, σ_i, has units of K^2.

The second criterion for evaluating the error between Eqs. 2 and 3 was relative percent error, χ, given by:

$$\chi_i = \frac{T_i - T_{\text{Ref}}}{T_{\text{Ref}}} \times 100 \quad (7)$$

where subscripts i and j are defined the same as in the sum squared of errors.

A third criteria was used to evaluate the overall correspondence between a description and a reference data sets. It was the coefficient of determination, $R_i^2 = 1 - \sigma_i / \sum_j \left(T_j - \bar{T}_{\text{Ref}}\right)^2$, where $\bar{T}_{\text{Ref}}$ is the mean of all the values of the reference temperature, and T_j represents the individual predicted temperatures of the model.

A minimum value obtained for the sum of squares of the temperature errors, σ_2, was taken as the best fit when parameters were estimated by fitting Eq. 2 to measured data. For example, the value of characteristic heat transfer length, L_{Air}, for experimental data was determined by fitting Eq. 2 to measured photocalorimetric data using the cooling portion of the temperature profile (where $\eta Q_{\text{I}} = 0$) in order to minimize σ_2. The effective power input to the cell, ηQ_{I}, was then determined using the value of L_{Air} derived from the cooling curve by minimizing σ_2 for the heating portion of the curve. When comparing Eqs. 3 and 2, the same values for ηQ_{I}, L_{Air}, and other physical parameters were used. Differences in thermal dynamics and equilibrium temperatures predicted by Eqs. 2 and 3 arose solely from the right-hand term in Eq. 4 into which a characteristic value of T' was inserted. T' was introduced in Eq. 5 and defined in terms of an optimum $f_{\Delta T}$. The sum-squared temperature error, σ_i, in Eq. 6 was used as the primary estimator for fit because it allowed for more precise comparison.

Results

Complete energy balance describes measured data

To evaluate application of the energy balance in Eq. 2 to the photocalorimetry data, predicted temperatures were compared to temperatures measured in the vacuum apparatus. Figure 3 compares photocalorimetric data with temperatures predicted by fitting Eq. 2 using L_{Air} in the cooling portion of the curve and ηQ_{I} in the heating portion of the curve. Predicted values deviate positively from experimental temperatures toward the tail of the cooling curve due to a small decrease in the ambient temperature, T_{Amb}, of the room induced by the automatic operation of the HVAC system. The sum-squared temperature error, σ_2, between Eq. 2 and the experimentally measured data was 1.26 K^2, and the coefficient of determination, R_2^2, was 0.998. Values of characteristic heat transfer length, L_{Air}, and effective power input, ηQ_{I}, that minimized the sum of squares of the errors, σ_2, were 24.6 mm and 2.53 mW, respectively.

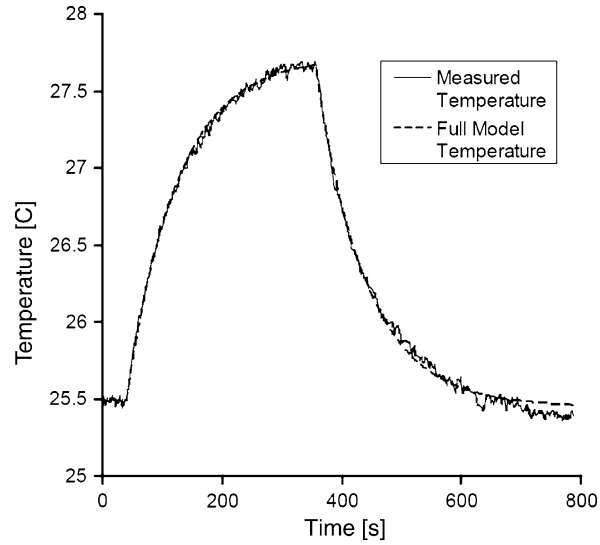

Fig. 3 Plasmon-resonant heating in a nanoparticle suspension due to laser irradiation beginning at 30 s, followed by cooling when irradiation is terminated at 350 s. Equation 2 was fit to experimental data, minimizing the sum-squared temperature errors, σ_2, defined by Eq. 6 in order to determine L_{Air} and ηQ_{I}. The sum-squared error was 1.26 K^2, and the coefficient of determination was 0.998. Values of L_{Air} and ηQ_{I} were 24.6 mm and 2.53 mW, respectively

Eighteen temperature profiles similar to Fig. 3. from five different photocalorimeter sample sets with nanoparticle concentrations ranging from 46 to 920 g Au/m^3 and characteristic heat transfer lengths from 4.1 to 66.8 mm were employed to examine applicability of Eq. 2. The heat transfer length, L_{Air}, in Eq. 2 that represents the characteristic distance for conduction by air, was adjusted to fit Eq. 2 to the cooling data. This accounted for deviations in sample cell size and orientation between the five sample sets. Standard deviations calculated from all replicates within each set relative to the mean value of L_{Air} were $\leq$30%. By setting the fitted value of L_{Air} constant during the heating curve, values of effective power input, ηQ_{I}, for the eighteen profiles were obtained, ranging from 1.0 to 16.3 mW. Minimum and maximum values of sum-squared error, σ_2, for comparing predicted vs. actual temperatures across the entire data set were 1.1 and 7.9 K^2, respectively, with an average of 2.90 $\pm$ 2.48 K^2 (one standard deviation). These correspond to coefficients of determination, R_2^2, from 0.982 to 0.998, with an average of 0.992 $\pm$ 0.007. Minimum and maximum values of relative percent error, χ_2, in predicted temperature vs. actual temperature over the entire set were $-$0.67 and 1.11%, respectively, with an average of 0.75 $\pm$ 0.22% for $|\chi_2|$. These criteria suggest Eq. 2 adequately describes transient thermal dynamics and steady-state temperature equilibria for the photocalorimetry data.

As an example, the fit shown in Fig. 3 yielded a value of $L_{\mathrm{Air}} = 24.6$ mm. The error associated with the change in ambient temperature at the distal end of the cooling curve comprises $\sim$ 30% of the total error. Figure 4 shows the relative percent error, χ_2, between measured temperature and temperatures predicted by Eq. 2 for the data in Fig. 3.

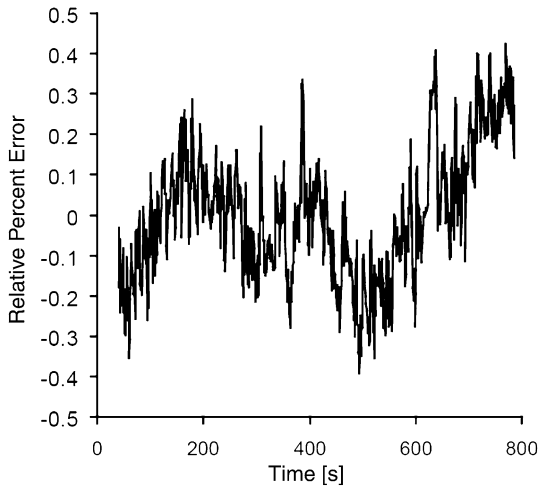

Fig. 4 A plot of the relative percent error, χ_2, between the full model, Eq. 2, and the measured data from the photocalorimetry experiment as seen in Fig. 3. The monotonic increase in error which begins at 500 s is due to a change in the ambient temperature, T_{Amb}, caused by the building's automated HVAC system

Linearized model approximates complete energy balance

We next assessed the degree to which the linear approximation accurately describes the complete energy balance as a function of the physical dimensions of the system, L_{Air}, and the effective energy input to the system, ηQ_{I}. Comparing the linearized model, Eq. 3, with the profile in Fig. 3 resulted in a sum-squared temperature error, σ_3, of 1.27 K^2, and a coefficient of determination, R_3^2, of 0.998. The sum of squares of the error is slightly higher than the value of $\sigma_2 = 1.26$ K^2 obtained using Eq. 2 and suggests Eq. 3 describes the profile in Fig. 3 with comparable accuracy. The profile generated using Eq. 3 employs the optimum $f_{\Delta T}$ of 0.8. The process used to determine the optimum $f_{\Delta T}$ value is described next.

The optimum $f_{\Delta T}$ value was determined by performing 378 simulations of both Eqs. 2 and 3 for characteristic heat transfer lengths, L_{Air}, from 1.5 to 393.6 mm and effective power inputs, ηQ_{I}, from 11.4 to 102.1 mW. These values produced temperature increases, ΔT, ranging from 3 to 77 °C. This span of simulated parameter values includes the range of photocalorimeter L_{Air} values (4.1–66.8 mm) as well as values <½ the minimum and >6 times the maximum of this range. Experimental ηQ_{I} values produced in the photocalorimeter ranged from 1.0 to 16.3 mW. The simulated ηQ_{I} range included the upper portion of these values and extended it by a factor of over 6 times the maximum. It was shown in the previous section that at temperature increases <3 °C, as in Figs. 3 and 4, the error between the Eqs. 2 and 3 is negligible.

We examined values of $f_{\Delta T}$ from 0.5 to 1.0 to find an optimum value that minimized χ_3. Figure 5 is a plot of the absolute value of the maximum percent relative error, χ_3, as a function of effective laser-power input, ηQ_{I}, for $f_{\Delta T}$ values increasing from 0.5 to 1.0. The characteristic length, L_{Air}, in this calculation was 24.6 mm. The lowest values of the absolute value of the maximum relative error, $|\chi_3|$, resulted at $f_{\Delta T} = 0.8$ as shown by the solid triangles. The value of $|\chi_3|$ increased as $f_{\Delta T}$ deviated from 0.8. The optimum value of $f_{\Delta T} = 0.8$ provided the smallest absolute value of the maximum relative percent error, $|\chi_3|$, over this broad range of parameters. Although introducing T_{Equil} into Eq. 4 by defining T' as in Eq. 5 requires specifying T_{Equil} in advance (from data or simulation), the resulting linearized form in Eq. 3 simplifies estimation of parameters from experimental data and gives a minimum-error linear driving force approximation of heat transfer in plasmon-resonant heating systems.

Next we assessed the accuracy of the linear model over the entire of range of conduction lengths, L_{Air}, and transduced power inputs, ηQ_{I}. Figure 6 shows the absolute value of the maximum relative error, $|\chi_3|$ plotted as a function of L_{Air} from

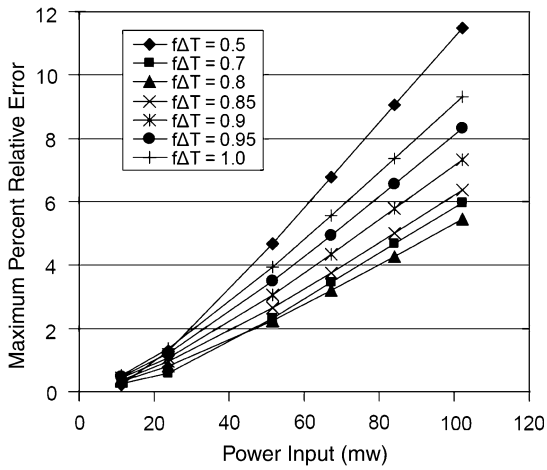

Fig. 5 A plot of the absolute value of the maximum relative percent error, $|\chi_3|$, with respect to transduced power input to the sample cell, ηQ_I, and the fraction of temperature increase, $f_{\Delta T}$, at a standard characteristic heat transfer length, L_{Air}, of 24.6 mm. An $f_{\Delta T}$ of 0.8 resulted in the smallest maximum error. The figure uses maximum χ_3 as found in Eq. 7 between the models, Eqs. 2 and 3

1.5 to 393.6 mm and ηQ_I from 11.4 to 102.1 mW using $f_{\Delta T} = 0.8$. This range of parameters included values used in photocalorimetry experiments ($4.1 \leq L_{Air} \leq 66.8$ mm, $1.0 \leq \eta Q_I \leq 16.3$). Within this narrow range the maximum $|\chi_3|$ was $\leq$1.5%. As air conduction length, L_{Air}, decreases below 3 mm, the error decreases monotonically to a negligible amount as conduction approaches and ultimately exceeds radiation as the predominant heat transfer mode. For $L_{Air} \leq 3$ mm, linearly approximating radiation results in negligible error. For $3 < L_{Air} \leq 200$ mm, the error of the approximation is affected by both heat transfer length and transduced power input. For $L_{Air} > 200$ mm, the maximum relative error, χ_3, was essentially a function of only ηQ_I.

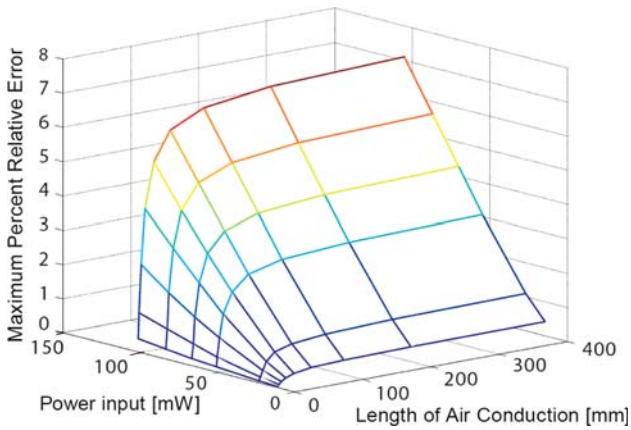

Fig. 6 A plot of the absolute value of the maximum percent relative error, $|\chi_3|$, with respect to the transduced power input, ηQ_I, and the length of air conduction, L_{Air}. For the experimental temperature data, the transduced power input ranged from approx. 1.0–16.3 mW and the L_{Air} was between 4.1 and 66.8 mm. As seen in the plot the error associated with this range was <1.5%

Applying linear description to DNA hybridization

One application of generating heat by transducing laser light via surface plasmons might be to thermally cycle nucleic acid hybridization on a DNA sensor. Complementary DNA strands are completely denatured at 95 °C, which is a 70 °C increase from ambient conditions [11]. Complementary DNA strands anneal without producing mismatch errors at approximately 55 °C. A temperature change of 40 °C is required to move from 55 to 95 °C during cycling. We evaluated errors between temperatures predicted with Eqs. 2 and 3, respectively, for ΔT values of 40 and 70 °C. Equations 2 and 3 allowed for determination of the effective power input required to achieve these ΔT values for a given heat transfer length. From Eq. 2 we found that to attain these equilibrium temperature changes required effective power inputs of 51.6 and 102.1 mW for the 40 and 70 °C increases, respectively. The simulations were performed with a characteristic heat transfer length of 2.5 cm (about 1 in.) and the errors associated with predicting a particular heating/cooling curve with Eqs. 2 and 3 were evaluated with Eqs. 6 and 7.

Figure 7 shows heating/cooling curves obtained using Eqs. 2 and 3 along with corresponding values of relative percent error for $\Delta T = 40$ °C (Fig. 7a, b) and $\Delta T = 70$ °C (Fig. 7c, d). Effective power input was initiated at $t = 0$ s and terminated at $t = 550$ s. Maximum values of relative percent error were −2.26% and −5.44% for $\Delta T = 40$ and 70 °C, respectively. The sum of squares of the errors, σ_3, for the 40 and 70 °C increases were 13.08 and 180.36 K^2, and coefficients of determination, R_3^2, were 0.9999 and 0.9993,

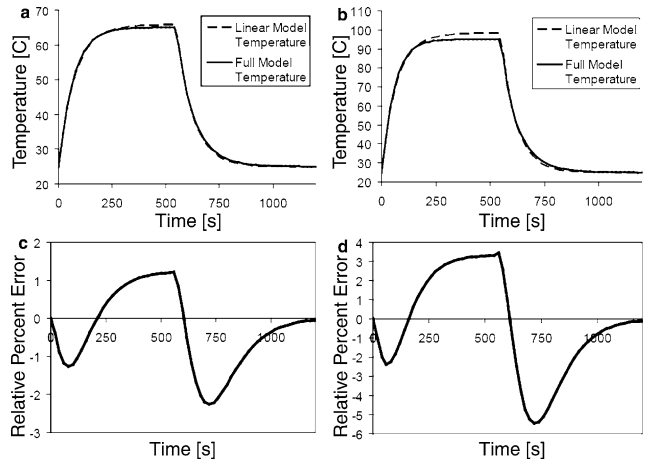

Fig. 7 A plot of the temperature profiles used to compare the linear, Eq. 3, to the full model, Eq. 2, and their respective relative percent differences, Eq. 7. Plots **a** and **b** are for the 40 °C temperature increase. Plots **c** and d are for the 70 °C temperature increase. The L_{Air} for **a**–**d** was set to 24.6 mm and the transduced power input, ηQ_I, for **a** and **b** was 51.6 mW whereas for **c** and **d** it was 102.1 mW. The sum of squares of the errors, σ_3, and coefficient of determination, R_3^2, was 13.08 K^2 and 0.9999 for the 40 °C and 180.36 K^2 and 0.9993 for the 70 °C, respectively

respectively. The linear approximation underpredicts temperatures from the complete energy balance as heating begins and shortly after cooling begins when the characteristic temperature T', Eq. 5, inserted into the radiation term in Eq. 4 exceeds the actual temperature and overemphasizes effects of radiative heat loss. Similarly the linear approximation overpredicts equilibrium temperature during heating because the characteristic temperature driving radiative heat loss is about 20% smaller than the presumed equilibrium, T_{Equil}. Therefore at $L_{\text{Air}} = 24.6$ mm and $\eta Q_{\text{I}} = 51.6$ and 102.1 mW, Eq. 3 could be successfully applied to DNA hybridization-based sensors with relatively modest error.

Figure 6 shows that errors in characterizing DNA hybridization sensors at $\eta Q_{\text{I}} = 51.6$ and 102.1 mW will change as the characteristic heat transfer dimension of the sensor changes. Equations 2–4 indicate that equilibrium temperature also changes for a given value of ηQ_{I} as L_{Air} changes. For example, decreasing L_{Air} to 1.5 mm at $\eta Q_{\text{I}} = 51.6$ mW yields a $\Delta T = 13.6$ °C with a maximum $|\chi_3| = 0.15\%$. At $\eta Q_{\text{I}} = 102.1$ mW a $\Delta T = 26.5$ °C is obtained with a maximum $|\chi_3| = 0.37\%$. Increasing L_{Air} to 393.6 mm at $\eta Q_{\text{I}} = 51.6$ mW yields a $\Delta T = 44.8$ °C with a maximum $|\chi_3| = 3.13\%$. At $\eta Q_{\text{I}} = 102.1$ mW, $\Delta T = 76.6$ °C is observed along with a maximum $|\chi_3| = 7.16\%$. Equations 2–7 can be applied to quantitate the accuracy of linearizing the overall energy balance in order to simplify data interpretation and analysis in a variety of microfluidic or lab-on-chip devices.

Conclusion

A continuum energy balance accurately describes thermal dynamics of plasmon resonant nanoparticle suspensions with heat transfer lengths from 4.1 to 66.8 mm that are irradiated by effective resonant light intensities between 1.0 and 16.3 mW to yield steady-state equilibrium temperature increases up to 10.6 °C. Sum-squared temperature errors in this range vary from 1.1 to 7.9 K^2 with an average value of 2.90 ± 2.48 K^2 ($N = 18$). Coefficients of determination, R_2^2, vary from 0.982 to 0.988 with an average value of 0.992 ± 0.007. Relative percent errors in temperature vary across the same range from −0.67 to 1.11%, with the absolute values averaging $0.75 \pm 0.22\%$ ($N = 18$). Parametric analysis of experimental data using the energy balance is simplified by introducing a characteristic temperature into a linear driving force approximation for radiative heat transfer. The characteristic temperature was defined in terms of a fractional approach to equilibrium. An optimum value of 0.8 for the fractional approach minimized maximum percent relative error to values $\leq$7.16% over a range of heat transfer lengths from 1.5 to 393.6 mm and a range of effective laser intensities from 11.4 to 102.1 mW that gave temperature increases from 3.0 to 76.6 °C.

The continuum energy balance and its linearized approximation were used to describe heating and cooling curves in plasmon-resonant DNA-hybridization sensors for temperature increases of 40 and 70 °C, respectively. Comparing the linearized and complete expressions gave maximum percent relative errors of −2.26% for the 40 °C increase and −5.44% for the 70 °C increase. Based on an analysis of photocalorimetric data it appears these expressions will be useful to describe and predict thermal dynamics and steady-state equilibrium temperatures in plasmon-resonant sensors, actuators and calorimeters across a wide range of geometries and operating conditions and will have application to microfluidic devices and lab-on-chips.

Acknowledgements This work was supported in part by NSF (NER) ECCS-0709456 and by NSF CMMI-0909749. The authors would like to acknowledge Ms. Wonmi Ahn for technical assistance.

References

1. Xue M, Li J, Xu W, Lu Z, Wang KL, Ko PK, Chan M. A self-assembly conductive device for direct DNA identification in integrated microarray based system, IDEM '02 Digest. IEEE International Electron Devices Meeting, San Francisco, CA, USA, Dec. 8–11, 2002, p. 207–10.
2. Storhoff JJ, Elghanian R, Mucic RC, Mirkin CA, Letsinger RL. One-pot colorimetric differentiation of polynucleotides with single base imperfections using gold nanoparticle probes. J Am Chem Soc. 1998;120(9):1959–64.
3. Kneipp K, Haka AS, Kneipp H, Badizadegan K, Yoshizawa N, Boone C, et al. Surface-enhanced Raman spectroscopy in single living cells using gold nanoparticles. Appl Spectrosc. 2002;56(2):150–4.
4. Kniepp K, Kniepp H, Manoharan R, Hanlon EB, Itzkan I, Dasari RR, et al. Extremely large enhancement factors in surface-enhanced Raman scattering for molecules on colloidal gold clusters. Appl Spectrosc. 1998;52(12):1493–7.
5. Ahmadi TS, Logunov SL, El-Sayed MA. Picosecond dynamics of colloidal gold nanoparticles. J Phys Chem. 1996;100(20):8053–6.
6. Logunov SL, Ahmadi TS, El-Sayed MA, Khoury JT, Whetten RL. Electron dynamics of passivated gold nanocrystals probed by subpicosecond transient absorption spectroscopy. J Phys Chem B. 1997;101(19):3713–9.
7. Link S, El-Sayed MA. Optical properties and ultrafast dynamics of metallic nanocrystals. Annu Rev Phys Chem. 2003;54(1):331–66.
8. Roper DK, Ahn W, Hoepfner M. Microscale heat transfer transduced by surface plasmon resonant gold nanoparticles. J Phys Chem C. 2007;111(9):3636–41.
9. Incropera F, DeWitt D. Fundamentals of heat and mass transfer. 5th ed. Hoboken: Wiley; 2002. p. 699–756, 905–932 (Chapter 12, Appendix A).
10. Roper M, Easley C, Legendre L, Humphrey J, Landers J. Infrared temperature control system for a completely noncontact polymerase chain reaction in microfluidic chips. Anal Chem. 2007;79(4):1294–300.
11. Eeles R, Stamps A. Polymerase chain reaction (PCR) the technique and its applications. Boca Raton: CRC Press; 1993. p. 4–11 (Chapter 2).
12. Lindfield G, Penny J. Numerical methods using Matlab. 2nd ed. Upper Saddle River: Prentice Hall; 2000, p. 200–249, 305.